Supporting Information

Promoting Sulfur Redox Kinetics of Atomically Dispersed Fe-NC Electrocatalyst by Carbon Vacancy toward Robust Lithium-Sulfur Batteries

Jie Zhang,[a] Dawei Yang,[,a,f] Canhuang Li,[b] Qianhong Gong,[a] Wei Bi,[a] Wei-Hong Lai,[c] Shengjun Li,[a] Yaojie Lei,*[,c] Guangmin Zhou,*[,d] Andreu Cabot*[,b,e] Guoxiu Wang,*[,c]*

[a] *Henan Key Laboratory of Quantum Materials and Quantum Energy, School of Quantum Information Future Technology, Henan University, Kaifeng, 475004, China.*

[b] *Catalonia Institute for Energy Research - IREC, Sant Adrià de Besòs, Barcelona, 08930, Spain.*

[c] *Centre for Clean Energy Technology Faculty of Science, University of Technology Sydney, Sydney, NSW, 2007, Australia.*

[d] *Tsinghua-Berkeley Shenzhen Institute & Tsinghua Shenzhen International Graduate School, Tsinghua University, Shenzhen, 518055 P. R. China.*

[e] *ICREA, Pg. Lluís Companys 23, 08010 Barcelona, Spain.*

[f] *Lead contact.*

Experimental Procedures

Chemicals

The chemicals used in this work such as methanol (99%), zinc nitrate hexahydrate ($Zn(NO_3)_2 \cdot 6H_2O$), iron sulfate heptahydrate ($FeSO_4 \cdot 7H_2O$), poly(vinylpyrrolidone) (PVP, Mw ≈ 50 000) and 2-methylimidazole were purchased from Sigma-Aldrich and used as received without any further purification. Washing was achieved with ultrapure water and reagent-grade ethanol and methanol where required. Ultrapure water was used for solution preparations.

Synthesis of ZnFe-ZIF

$Zn(NO_3)_2 \cdot 6H_2O$ (0.575 g) and $FeSO_4 \cdot 7H_2O$ (0.019 g) were dissolved into 50 mL of methanol to form a solution. 50 mL of methanol containing 2-methylimidazole (0.66 g) and PVP (0.6 g) were poured into $Zn(NO_3)_2$ and $FeSO_4$ solution. The mixture was kept stirring at room temperature for 24 h. The resulting white precipitates were collected by centrifugation, washed with methanol three times, and finally dried at 80 °C overnight.

Synthesis of Hollow ZIF Materials

10 mL methanol solution containing 100 mg ZnFe-ZIF nanocrystals was incubated in 40 mL of a tannic acid solution (8 g L^{-1}) and aged for 10 min. The hollow ZIF materials were collected by centrifugation and washed with methanol three times, and finally dried at 80 °C overnight.

Synthesis of Single-Atom Catalysts

The as-prepared ZIF nanoparticles were carbonized in flowing Ar in a tube furnace using a heating rate of 2 °C min^{-1} up to 800 °C, and dwell for 3 h.

Materials Characterization

X-ray diffraction (XRD) patterns were performed using a Bruker AXS D8 Advance X-ray diffractometer with Cu K radiation (λ = 1.5106 Å) operating at 40 kV and 40 mA. Field emission scanning electron microscopy (FE-SEM, ZEISS Auriga) equipped with an energy dispersive X-ray spectroscopy (EDX). High-resolution TEM (HRTEM) studies were carried out to characterize the morphology/structure and composition of the samples using a FEI Tecnai F20 microscope at 200 kV. High-angle annular dark-field scanning transmission electron microscopy (HAADF-STEM) images and elemental mapping were obtained in a spherical aberration-corrected transmission electron microscope FEI Titan 80-300 at 300 kV and FEI Titan G2 80-200 ChemiSTEM with four EDX detectors or (Super-X) and operated at 200 kV.

X-ray photoelectron spectroscopy (XPS) measurements were carried out using 150 W and a Phoibos 150 MCD-9 detector. X-ray absorption near-edge structure (XANES) and extended X-ray absorption fine structure (FT-EXAFS) were performed at the Beijing Synchrotron Radiation Facility (BSRF). The obtained XAFS data were analyzed according to the standard procedures using ATHENA program. The content of sulfur within the cathode composites was estimated by thermogravimetric (TGA) on a PerkinElmer Diamond TG/DTA instrument under N2 at a heating rate of 10 °C min^{-1}. UV-vis absorption spectra were collected using PerkinElmer Lambda 950 UV-vis spectrophotometer. Nitrogen adsorption-desorption isotherms were recorded to calculate the specific surface area and analysis of the pore size distribution by Brunauer-Emmett-Teller method on a Tristar II 3020 Micromeritics system. All solid-state NMR experiments were acquired on a Bruker AVANCE NEO 600 MHz (14.1 T) spectrometer using a Bruker 3.2 mm HXY magic-angle-spinning (MAS) probe. The Larmor frequency for ^{13}C and ^{7}Li was determined as 150.94 MHz and 233.28 MHz, respectively. ^{13}C and ^{7}Li NMR spectra were acquired by using one pulse, referenced to adamantane at 38.5 ppm and 1 M LiCl solution at 0 ppm, respectively. The spinning rate ν_{rot} was set to 18 kHz and all measurements were carried out at room temperature. EPR measurements were carried out on a CIQTEK EPR200-Plus spectrometer equipped with a high-sensitivity cavity in the X-band. The spectra were acquired at room temperature (RT) with an incident microwave power of ~0.2 mW.

Li-S Cell Assembly and Measurements

S@host composites (S@Fe-SAs/N-C_v, and S@N-C), PVDF binders and Super P (weight ratio=8:1:1) were well mixed into NMP to form a black slurry, which was coated on Al foils and dried at 60 °C overnight. After drying, the coated Al foil was punched into small disks with a diameter of 12 mm. Sulfur loading was around 1.0-1.2 mg cm^{-2}. CR2032 coin-type cells were assembled, in which lithium foils were used as the anode, Celgard 2400 membranes as S4 separators, S@host composites as the cathode. and 1.0 M LiTFSI in DOL/DME solvent (1:1 vol%) with 0.2 M $LiNO_3$ additive as the electrolyte. For each coin cell, the electrolyte/sulfur ratio (E/S) was controlled to be about 20 μL mg^{-1}. The galvanostatic charge/discharge (GCD) measurements were performed with a voltage window of 1.7-2.8 V vs. Li^+/Li on a Neware BTS4008 battery tester at different C rates. The battery tester BCS-810 from BioLogic was used to carry out the cyclic voltammetry (CV) measurements at a scan rate of 0.1-0.4 mV s^{-1},

and the electrochemical impedance spectroscopy (EIS) tests were conducted with a voltage amplitude of 10 mV in the frequency range 100 kHz to 10 mHz.

Synthesis of Li_2S_4 solutions for adsorption test

Sulfur and Li_2S with a molar ratio of 3:1 dissolved in an appropriate amount of DME/DOL (volume ratio of 1:1) solution under vigorous magnetic stirring overnight, eventually obtaining a homogeneous dark brown solution. To evaluate the polysulfide adsorption ability, a certain amount of S@host composites (S@Fe-SAs/N-C_v, and S@N-C) were added to 3.0 mL 10 mM Li_2S_4 solution under Ar atmosphere, respectively.

Symmetric Cell Assembly and Measurements

Symmetric cells were also assembled and tested under CR2032 coin cells, in which two pieces of the same electrode (average loading about 0.5 mg cm^{-2}) were used as working and counter electrodes with 40 μL of electrolyte containing 0.5 mol L^{-1} Li_2S_6 and 1 mol L^{-1} LiTFSI dissolved in DOL/DME (v/v = 1/1). For comparison, symmetric cells in a Li_2S_6-free electrolyte were also assembled and tested under CR2032 coin cells. The CV measurements for all the symmetric cells were performed at a scan rate of 20 mV s^{-1} in a voltage window between -0.8 and 0.8 V.

Measurement of Nucleation of Li_2S

Nucleation of Li_2S was tested in 2032-coin cells to investigate the liquid-solid reaction kinetics. 1 mg of host materials was loaded on the carbon papers applied as working electrodes. Li foil worked as the counter electrode. The catholyte consisted of 20 μL of 0.25 M Li_2S_8 and 1.0 M LiTFSI in tetraethylene glycol dimethyl ether solution. In the case of anolyte, it contained 20 μL of a 1.0 M LiTFSI solution without Li_2S_8. The cells were first discharged at a current of 0.112 mA to 2.19 V and then hold the voltage at 2.05 V until the current decreased to 10^{-2} mA for Li_2S nucleation and growth.

DFT calculations

Density functional theory (DFT) calculations were performed using the VASP[1] package with VASPKIT[2] code for post-processing the calculated data.[1,2] Generalized gradient approximation (GGA) with the Perdew-Burke-Ernzerhof functional is employed to treat the exchange-correlation energy.[3] The interaction between core and valence electrons was described by the projected augmented wave (PAW) basis set.[4] A converged cutoff was set to 550 eV. Zero

damping DFT-D3 method was used to investigate weak intermolecular interactions.[5] 1/8 corrected (300 K) S_8 molecular energy and 1/4 bulk *Li* (4 atoms) crystal energy were used to do the process of energy subtraction of reaction free energy.

Adsorption energy was calculated by the following formula:

$$E_{\text{adsorption energy}} = E_{\text{Total}} - E_{\text{Molecule}} - E_{\text{Surf}}$$

Where E_{Total} and E_{Surf} are the total energies of Li-S battery electrode material adsorbed with and without polysulfide species Li_2S_x (x = 1, 2, 4, 6 and 8), and E_{Molecule} is the energy of the Li_2S_x. With this definition, the more negative the value, the stronger ability of Li-S battery electrode material to adsorb Li_2S_x. The molecular configuration of lithium polysulfides is shown in Fig. S9, the bond lengths are all within a reasonable range[8].

The band gap of Fe-SAs/N-C and Fe-SAs/N-C_v was calculated using CP2K[7], and the required input file for CP2K was generated through Multiwfn[9].

Transition states of interest were calculated by the climbing-image nudged elastic band (CI-NEB) method.

The Gibbs free energy of the discharging process from S_8 to Li_2S on the Fe-SAs/N-C_v was calculated following the reaction sequence:

$$S_8 + Li \rightarrow Li_2S_8 \rightarrow Li_2S_6 \rightarrow Li_2S_4 \rightarrow Li_2S_2 \rightarrow Li_2S$$

$\Delta G = \Delta E + \Delta ZPE - \Delta TS$

Where ΔG, ΔE, ΔZPE, and TS represented the free energy, total energy from DFT calculations, zero-point energy, and entropic contributions (T was set to be 300 K), respectively.

Thus, the binding energy of reactants and products (like $E^{Bind}_{Li_2S_6} - E^{Bind}_{Li_2S_4}$) certainly affect ΔE ($Li_2S_6 \rightarrow Li_2S_4$) and thus the value of ΔG, but a high binding energy does not always translate into a high Gibbs free energy change.

where $E_{Li_2S_x}$ is the energies of the LiPS.

The Gibbs free energy calculation and the Li_2S decomposition barrier calculation aim to verify that Fe-SAs/N-C_v, has good catalytic ability. A comparative analysis of the theoretical calculation results and experimental results from multiple articles further confirms that the theoretical calculation results align well with the experimental results (Tab. S3).

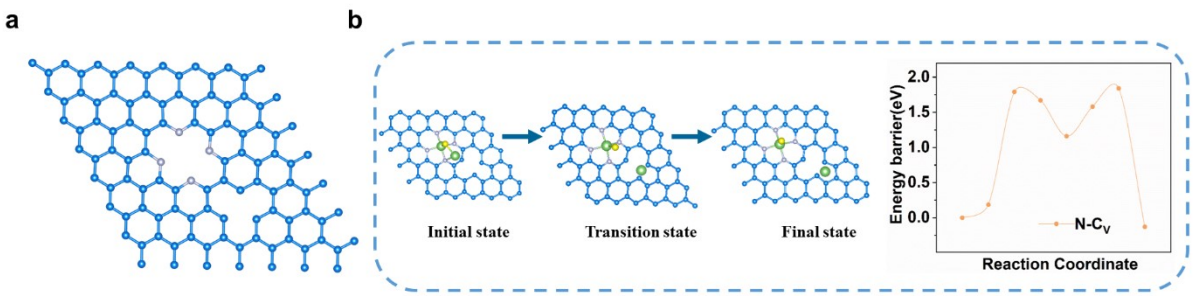

Fig. S1 (a) Structural features of N-C_v. (b) Decomposition energy barriers of Li_2S on N-C_v.

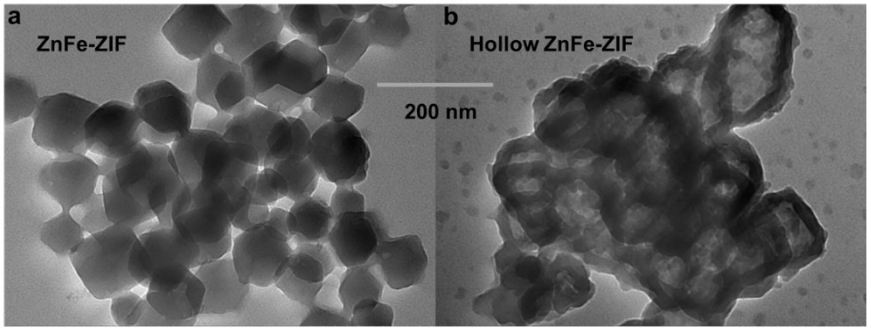

Fig. S2 (a) TEM images of ZnFe-ZIF. (b) TEM images of hollow ZnFe-ZIF.

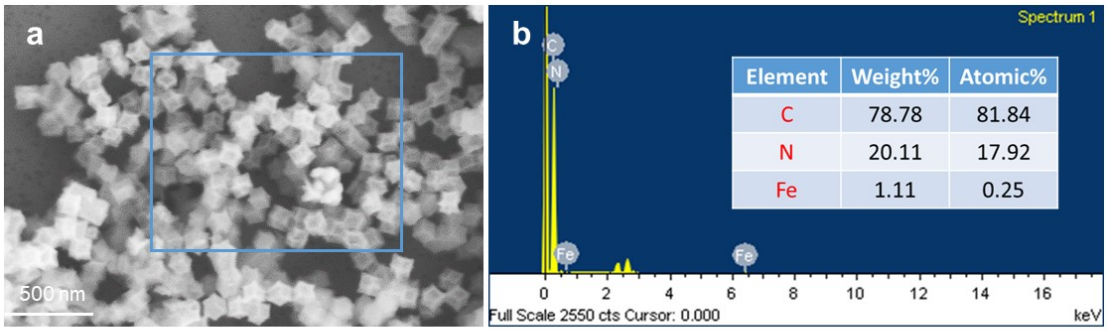

Element	Weight%	Atomic%
C	78.78	81.84
N	20.11	17.92
Fe	1.11	0.25

Fig. S3 (a,b) SEM image and EDX spectrum of Fe-SAs/N-C_v.

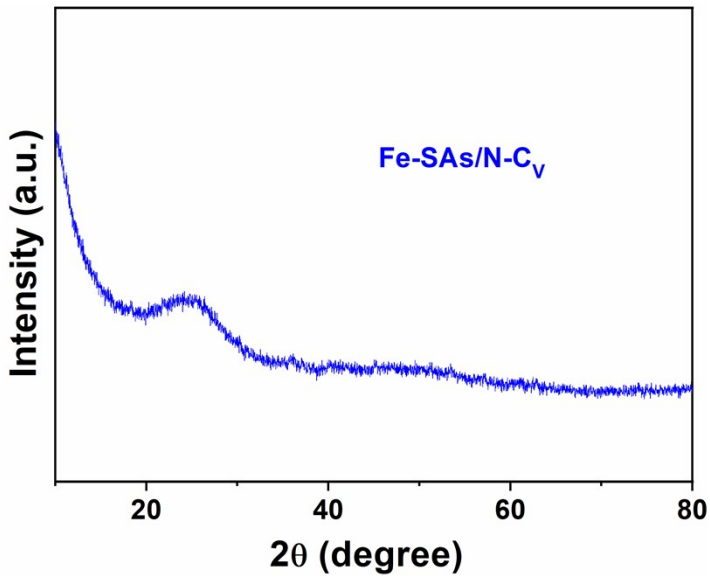

Fig. S4 XRD pattern of Fe-SAs/N-C_v.

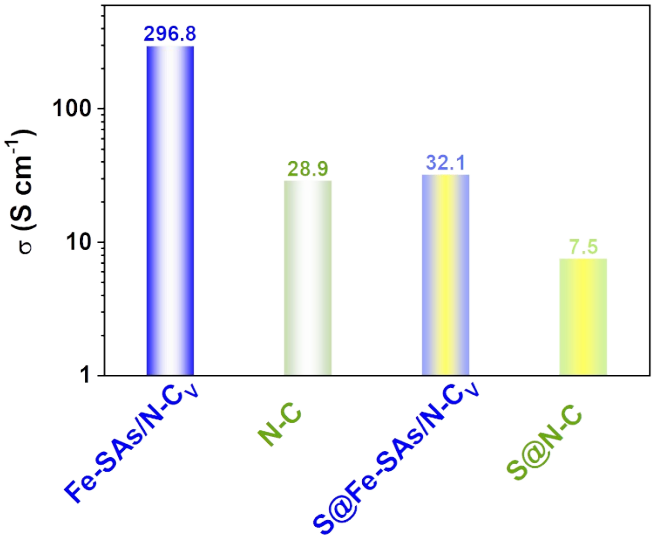

Fig. S5 Electrical conductivity of the two hosts (Fe-SAs/N-C_v and N-C) tested before and after fusion with sulfur.

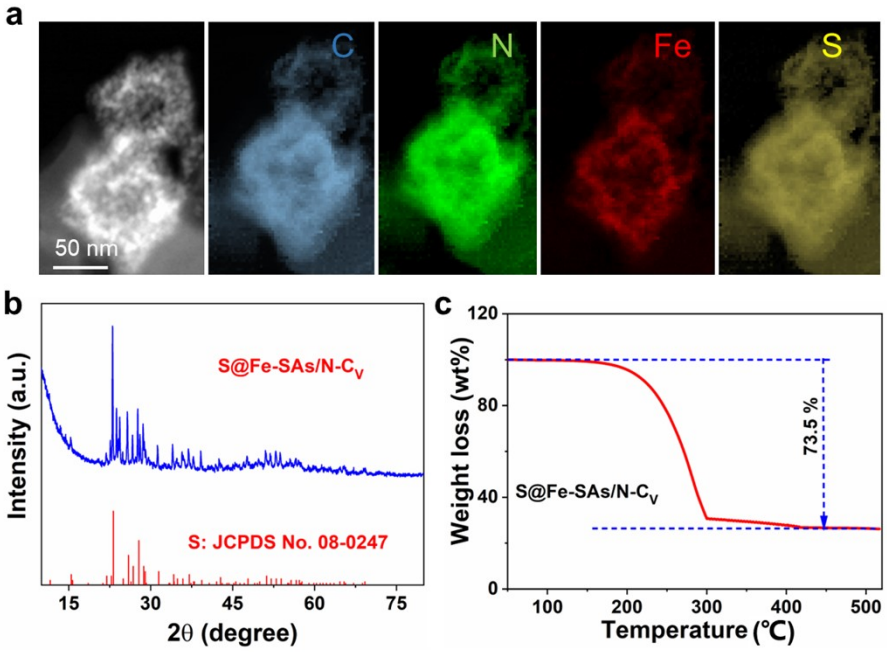

Fig. S6 (a) SEM-EDX compositional maps of S@Fe-SAs/N-C_v. SEM-EDX characterization of the obtained S@Fe-SAs/N-C_v composites confirmed the presence of S homogeneously distributed within the host material. (b) XRD pattern of S@Fe-SAs/N-C_v. XRD patterns further showed the presence of crystalline sulfur (JCPDS No. 08-0247) within S@Fe-SAs/N-C_v. (c) TGA curves of S@Fe-SAs/N-C_v.

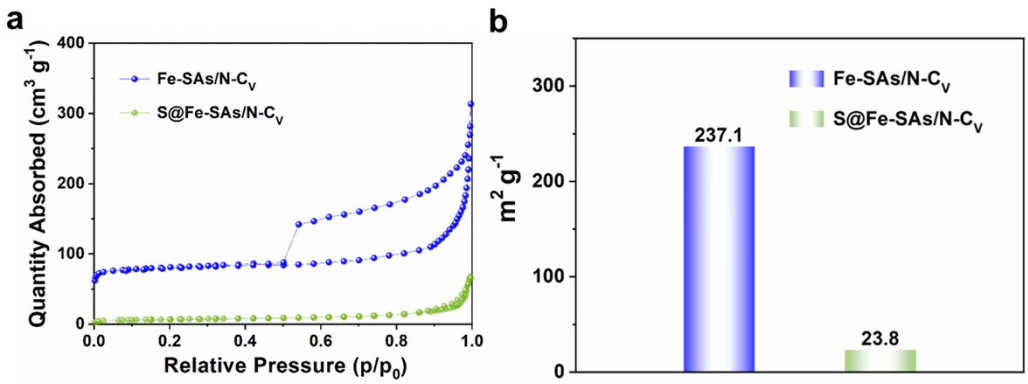

Fig. S7 (a,b) N_2 adsorption-desorption isotherms of Fe-SAs/N-C_v and S@Fe-SAs/N-C_v. With the introduction of sulfur, the Brunauer–Emmett–Teller (BET) specific surface area of the material sharply decreased from 237.1 m^2 g^{-1} (Fe-SAs/N-C_v) to 23.8 m^2 g^{-1} (S@Fe-SAs/N-C_v).

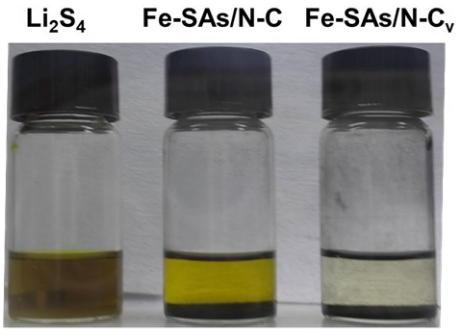

Fig. S8 Optical photograph of the flasks containing a Li_2S_4 solution and the different materials after overnight adsorption.

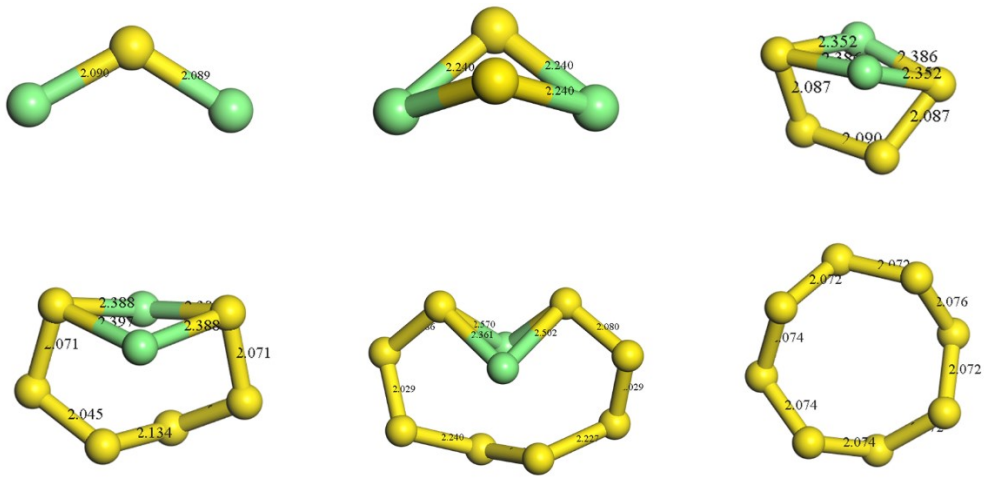

Fig. S9 Li_2S_n (n = 1, 2, 4, 6, 8) and S_8 molecule.

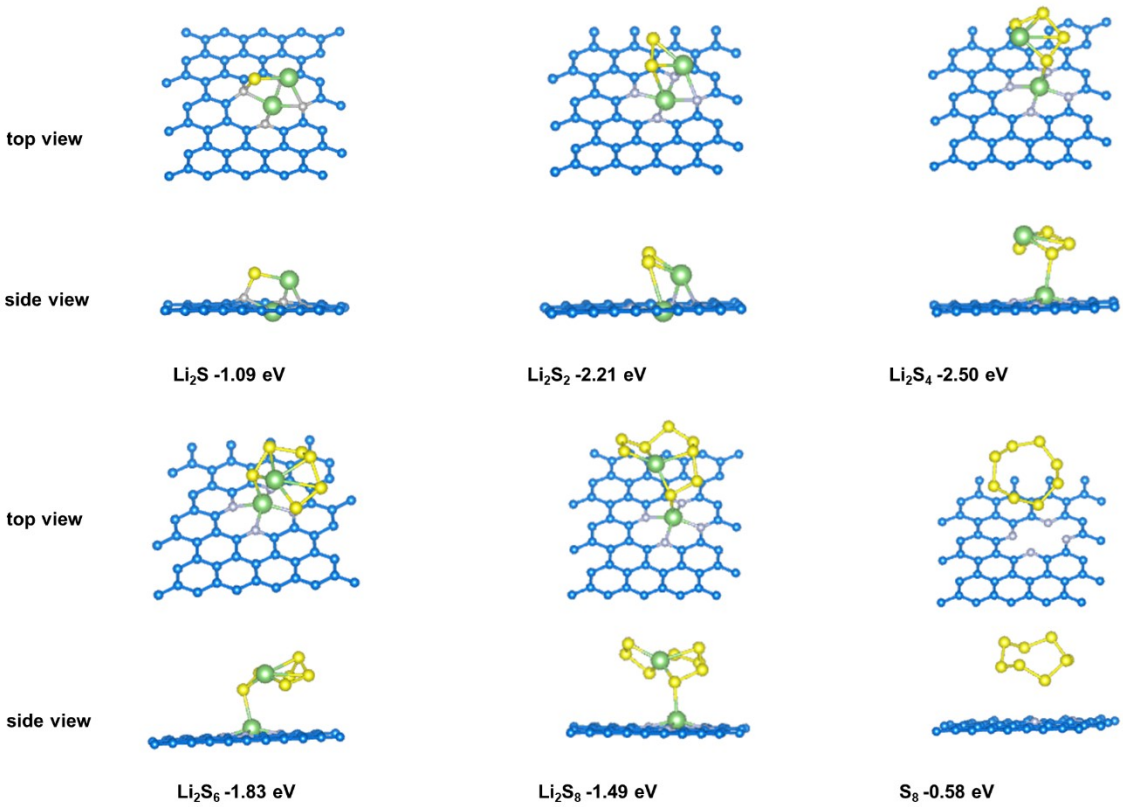

Fig. S10 Adsorption energy and adsorbed structures of LiPS on the surface of N-C calculated by DFT.

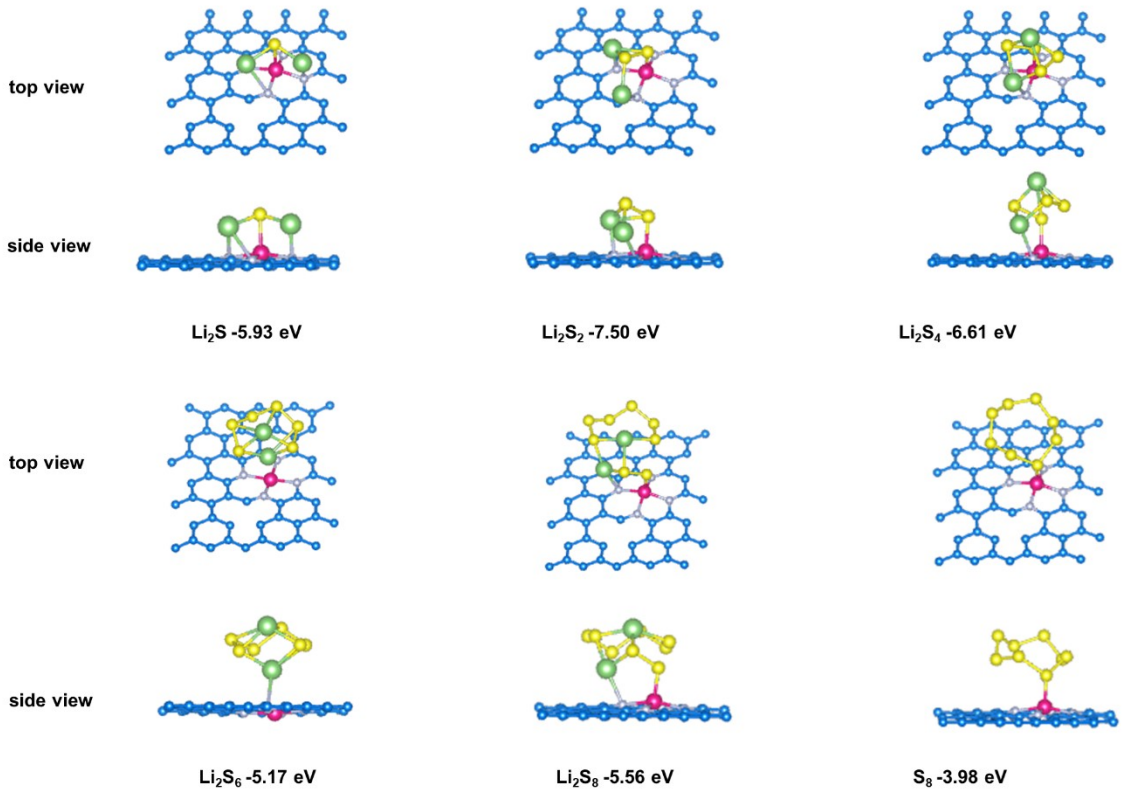

Fig. S11 Adsorption energy and adsorbed structures of LiPS on the surface of Fe-SAs/N-C_v calculated by DFT.

Fig. S10 and S11 exhibit the optimized adsorption configuration of LiPS species on N-C and Fe-SAs/N-C_v at six different lithiation stages (Li_2S, Li_2S_2, Li_2S_4, Li_2S_6, Li_2S_8 and S_8). The Li and S atoms of Li_2S_x species can form chemical bonds with N and Fe atoms in N-C and Fe-SAs/N-C_v, respectively, attributed to the coupling between Lewis acids (Li and Fe atoms with unoccupied orbitals) and Lewis bases (N and S atoms with lone electron pairs).

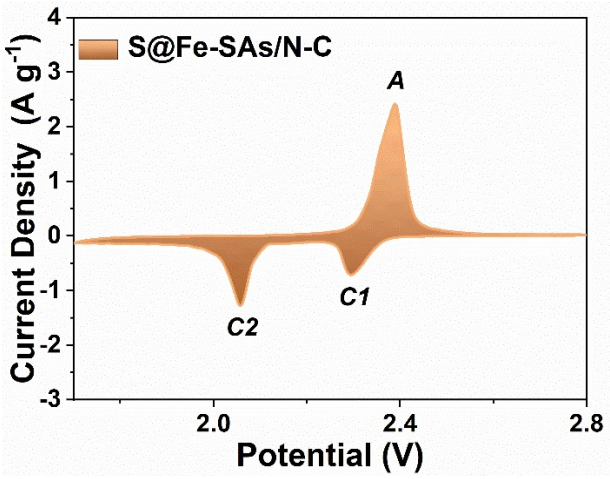

Fig. 12 CV curves of Li-S coin cells at a scan rate of 0.1 mV s^{-1}.

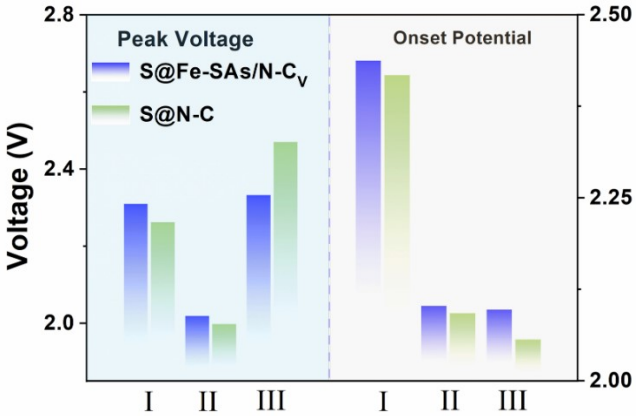

Fig. S13 Peak voltages and onset potentials of Li-S batteries based on CV curves.

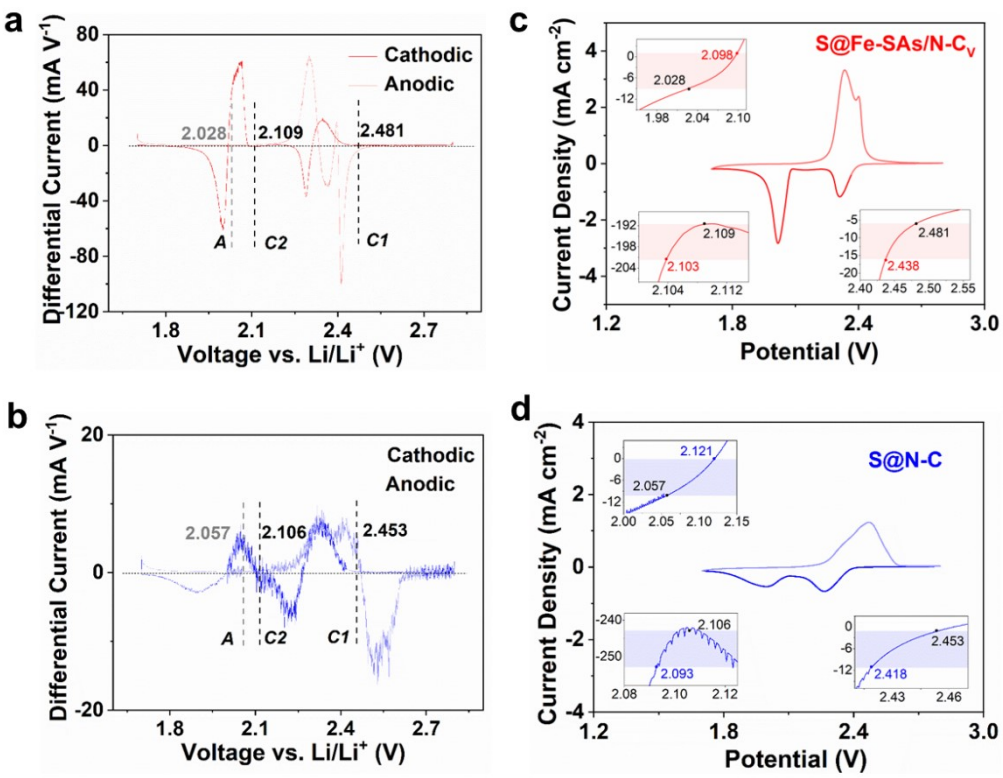

Fig. S14 Onset potential for Li-S redox reactions. (a,b) Differential CV curves of S@Fe-SAs/N-C_v a) and S@N-C (b). The baseline voltage and current density are defined as the value before the redox peak, where the variation in current density is the smallest, namely dI/dV = 0. Baseline voltages are denoted in black for cathodic peaks C1, C2, and in gray for anodic peak A, respectively. (c,d) CV curves an corresponding onset potentials of redox peak I, II, and III (inset): c) S@Fe-SAs/N-C_v, (d) S@ N-C.

Following a common definition employed in electrocatalysis, the onset potential is determined when the current density is 10 μA cm^{-2} beyond the corresponding baseline current density (more specifically, 10 μA cm^{-2} more negative than baseline current density for cathodic peaks or 10 μA cm^{-2} positive than baseline current density for anodic peaks). As shown in the inset of c and d, the baseline voltages are the same as in a and b, while the colored region indicates the gap in current density (10 μA cm^{-2}).

The catalytic activity of Fe-SAs/N-C_v electrodes was quantified through the onset potential at a current density of 10 μA cm^{-2} beyond the baseline current (Fig. S14). The cells based on S@Fe-SAs/N-C_v electrodes were characterized by higher/lower onset potentials for cathodic/anodic peaks, demonstrating faster redox kinetics for the LiPS conversion reaction.

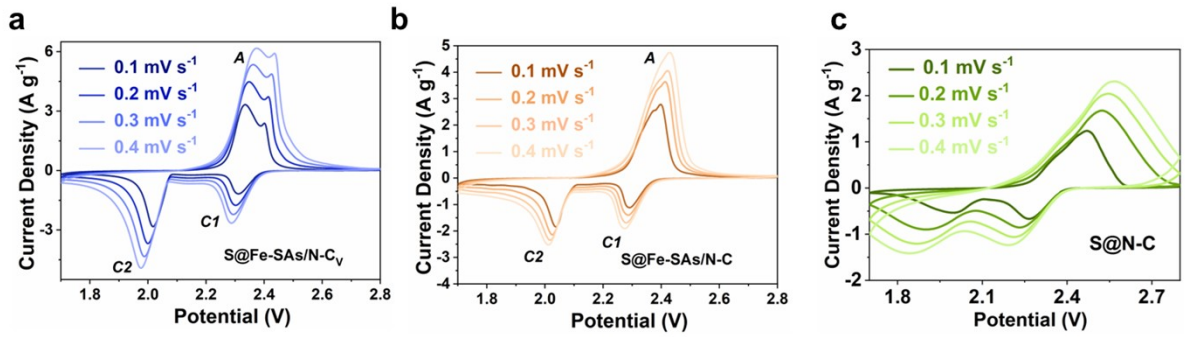

Fig. 15 (a) CV curves of S@Fe-SAs/N-C_v at different scan rates. (b) CV curves of S@Fe-SAs/N-C at different scan rates. (c) CV curves of S@N-C at different scan rates.

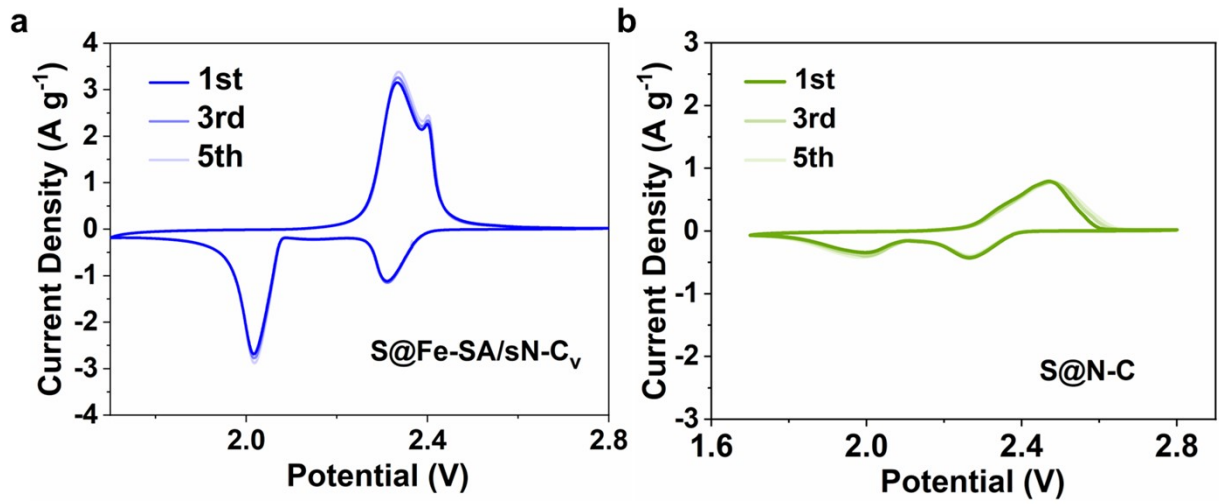

Fig. S16 First three cycles of CV curves of (a) S@Fe-SAs/N-C_v, and (b) S@N-C performed at a scan rate of 0.1 mV s^{-1}. The CV curves measured from S@Fe-SAs/N-C_v cathodes almost overlapped during the first three cycles, indicating good reversibility of the sulfur redox reactions.

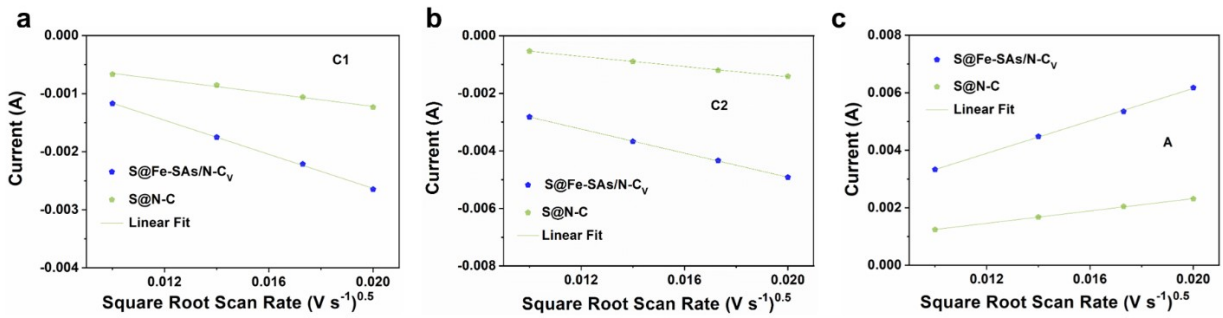

Fig. S17 (a) Plots of CV peak current for the first cathodic reduction, (b) the second cathodic reduction, (c) anodic oxidation process vs. the square root of the scan rates.

The Randles-Sevcik equation was used to calculate the diffusion constant of lithium ions (D_{Li+}) in the process:

$$I_p = (2.69*10^5)n^{1.5}AD_{Li+}^{0.5}C_{Li+}v^{0.5}$$

Where I_p is the peak current (taken as the ceter of the current band in the case of III), n represents the number of charge transfer, A is the geometric electrode area, C_{Li+} is the concentration of Li^+, and v is the scan rate. A, n, and C_{Li+} are constant in this equation, thus the sharper $I_p/v^{0.5}$ slopes, the faster Li^+ diffusion. As plotted in Fig. S17a-c, compared with S@N-C, S@Fe-SAs/N-C_v electrodes exhibited the sharpest slopes among the three peaks, thus the highest Li^+ diffusivity during the redox reactions.

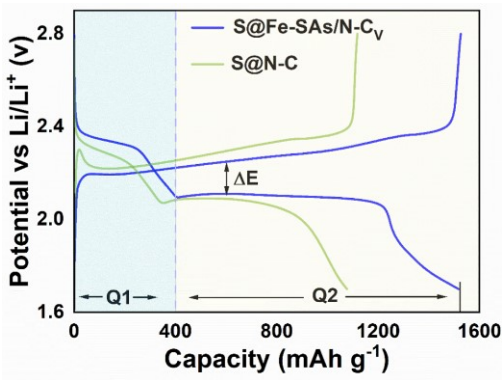

Fig. S18 Charge-discharge curves of each electrode at a current of 0.1 C.

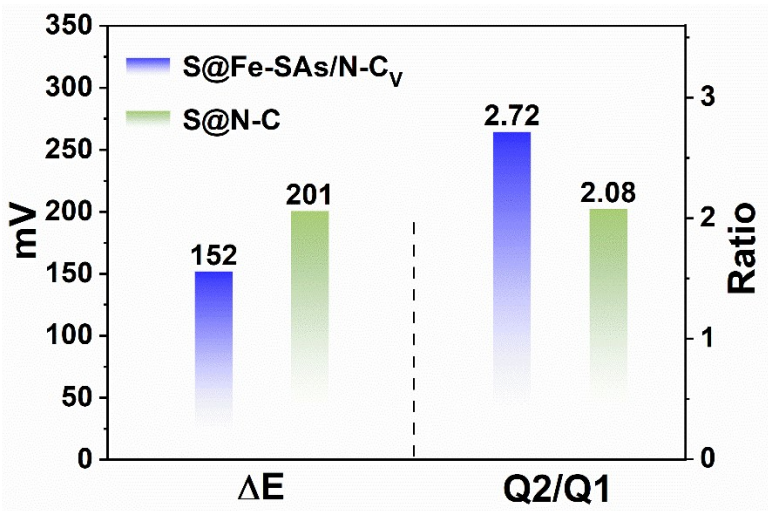

Fig. S19 Values of △E and Q2/Q1 obtained from charge/discharge profiles.

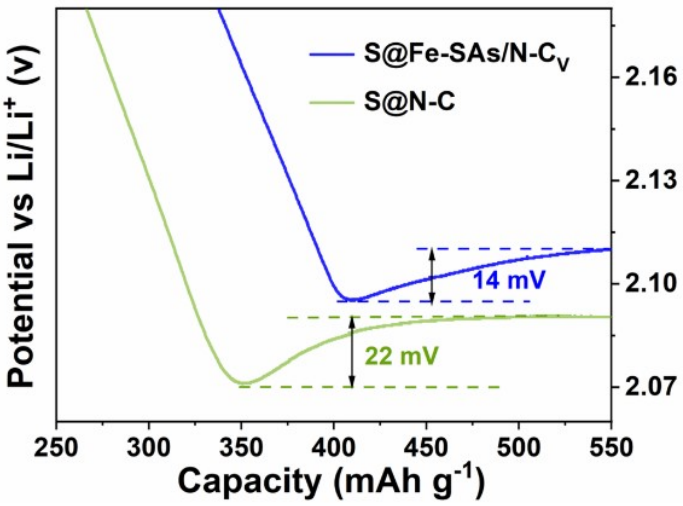

Fig. S20 Discharge curves of S@Fe-SAs/N-C_v and S@N-C electrodes.

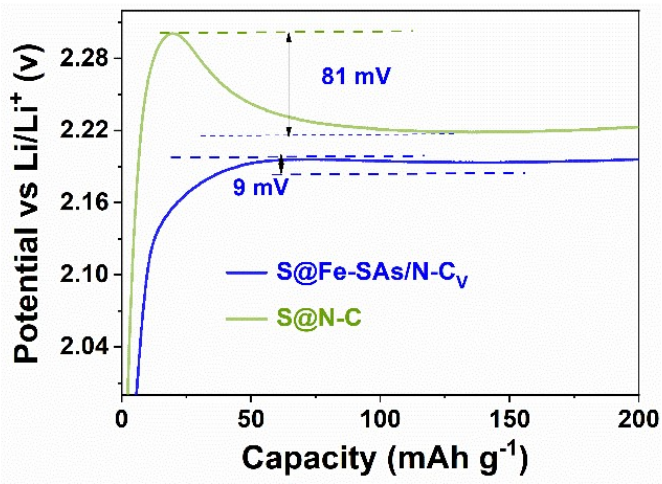

Fig. S21 Charge profiles of S@Fe-SAs/N-C_v, and S@N-C electrodes showing the overpotentials for conversion between soluble LiPS and insoluble Li_2S_2/Li_2S.

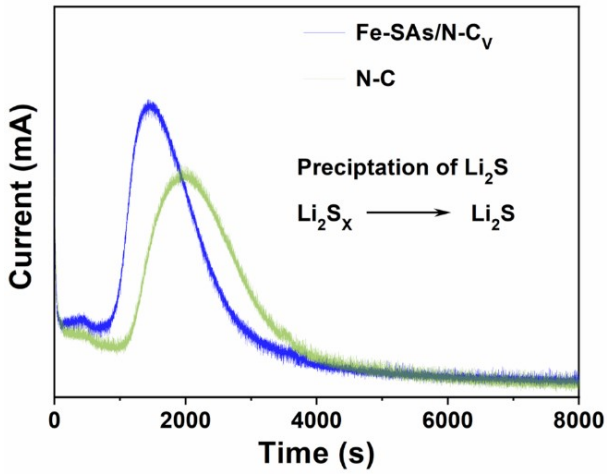

Fig. S22 Potentiostatic discharge curves of S@Fe-SAs/N-C_v and S@N-C electrodes with Li_2S_8 catholyte at 2.05 V.

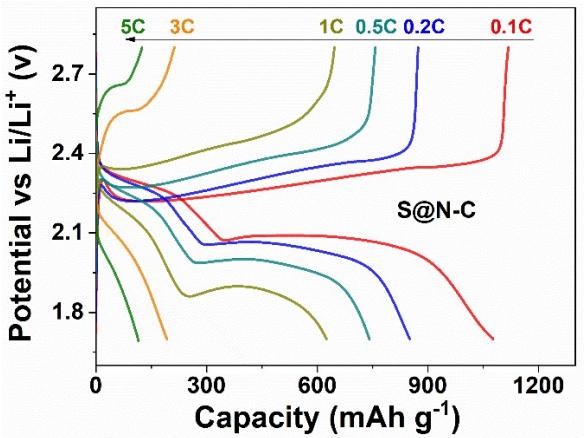

Fig. S23 Galvanostatic charge/discharge profiles of S@N-C electrodes at different current densities range from 0.1 C to 5 C.

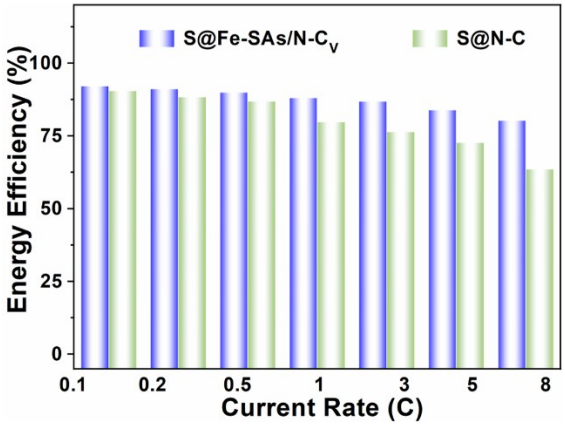

Fig. S24 Energy efficiency at various current rates for S@Fe-SAs/N-C_v electrodes.

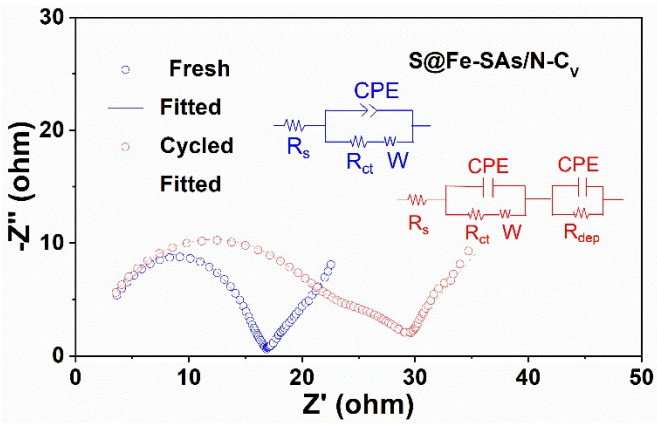

Fig. S25 EIS of S@Fe-SAs/N-C_v symmectic cells. The inset is the equivalent circuit.

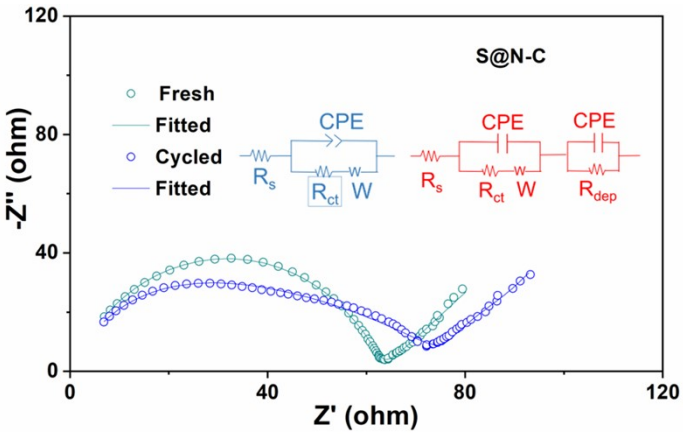

Fig. S26 EIS of S@N-C symmectic cells. The inset is the equivalent circuit.

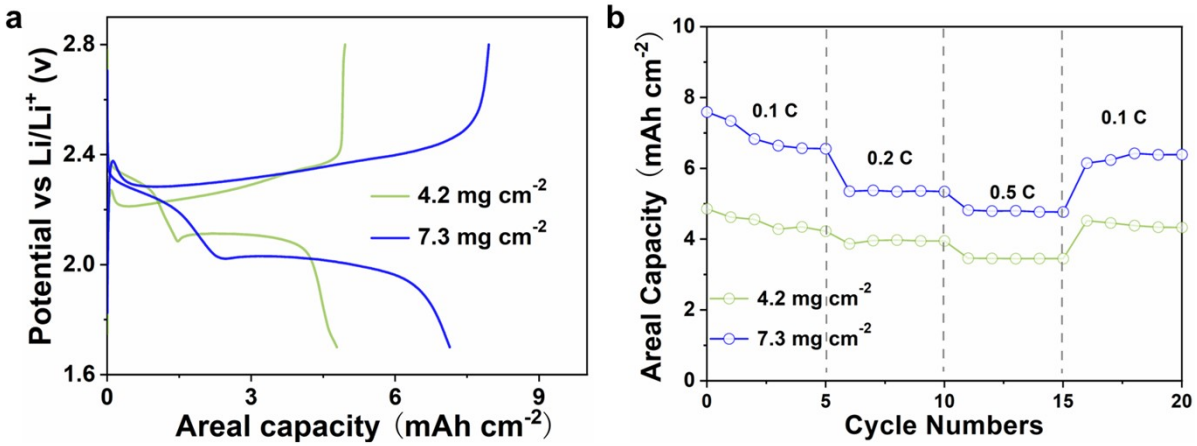

Fig. 27 (a) Galvanostatic charge/discharge profiles at 0.2 C with the sulfur loading of 4.2, and 7.3 mg cm^{-2}. (b) Rate capabilities of S@Fe-SAs/N-C_v electrodes.

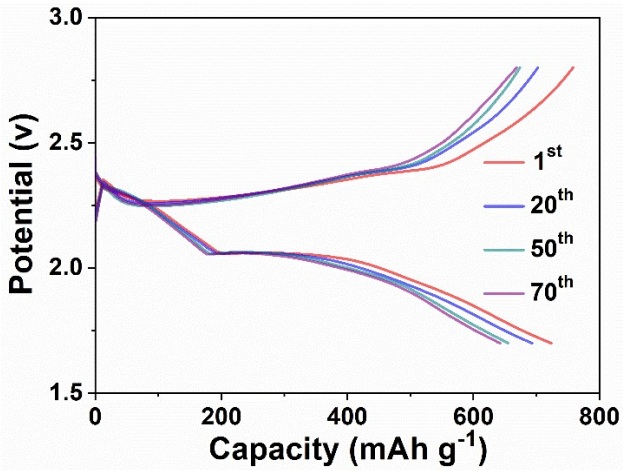

Fig. 28 Galvanostatic charge/discharge curves of Li-S pouch cell based on S@Fe-SAs/N-C_v electrodes.

Tab. S1 EXAFS fitting parameters at the Fe K-edge for Fe foil and Fe-N-C catalyst.

Sample	**Shell**	***N*** [a]	***R (Å)*** [b]	σ^2 **(Å²·10⁻³)** [c]	**Δ*E*⁰ (eV)** [d]	***R factor (%)***
Fe-N-C	Fe−N_1	2.1(±0.2)	1.96(±0.02)	3.7(±0.2)	-7.2	2.3
	Fe−N_2	2.0(±0.2)	1.86(±0.02)	6.4(±0.2)	-3.0	
Fe foil	Fe−Fe	8.0	2.47(±0.01)	4.2(±0.2)	7.2	0.2
	Fe−Fe	6.0	2.85(±0.01)	5.3(±0.2)	5.9	

a N: coordination number; b R: bond distance; c σ2: Debye-Waller factor; d ΔE0: the inner potential correction. R factor: goodness of fit. S02, 0.733, was obtained from the experimental EXAFS fitting over Fe foil with known crystallographic value, which was then used to all the samples

Tab. S2 Resistance of the insulating Li_2S_2/Li_2S layer deposited on the electrode surface (Rdep) during cycling, and charge transfer resistance (Rct) before and after cycling.

Electrodes	**Resistance (R_{ct}-Before)**	**Resistance (R_{dep})**	**Resistance (R_{ct}-After)**
S@Fe-SAs/N-C_V	13.5 Ω	18.02 Ω	5.98 Ω
S@N-C	55.7 Ω	46.9 Ω	19.6 Ω

Tab. S3 A comparison is made between the adsorption energy (E_{ads}) of Li_2S_4 or Li_2S_6 on electrode materials and the maximum difference in Gibbs free energy for the reactions progressing from S_8 to Li_2S on electrode materials, along with a correlation to the UV-vis absorption spectra and cyclic voltammetry (CV) data.

	Absorption ability		Catalytic performance		
Electrode material	**Cal.**	**Exp.**	**Cal.**	**Exp.**	**Ref**
	$-E_{ads}$ (Li_2S_4 or Li_2S_6)	**UV-vis spectra**	**ΔG**	**CV curves**	
NiB	≈-4.3(Li_2S_6)	High	1.12	Weak	10
P-NiB	≈-4.8(Li_2S_6)	Low	1.04	Strong	
NPS	≈0.7(Li_2S_6)	High	0.819	Weak	
CoSA-N_4	≈0.9(Li_2S_6)	Medium	0.814	Medium	11
CoSA-N_3PS	≈5.5(Li_2S_6)	Low	0.806	Strong	
NC	≈2.1(Li_2S_6)	High	1.097	Weak	
β-MO_2C	≈3.9(Li_2S_6)	Medium	0.677	Medium	12
δ-B-Mo_2C	≈4.2(Li_2S_6)	Low	0.587	Strong	
Ni-N_3-C	1.24(Li_2S_4)	High	0.727	Weak	13
Ni-N_3-NSC	1.55(Li_2S_4)	Low	0.599	Strong	
NC	≈0.25(Li_2S_6)	High	1.51	Weak	14
Nb-SAs@NC	≈3.8(Li_2S_6)	Low	1.02	Strong	
NiS_2	0.03(Li_2S_6)	High	0.86	Medium	
$NiSe_2$	0.17(Li_2S_6)	Medium	0.92	Weak	15
NiS_2/ $NiSe_2$	0.22(Li_2S_6)	Low	0.87	Strong	

Tab. S4 A comprehensive comparison of the electrochemical performance of the Fe-SAs/N-C_v host in this work with metal atom-dispersed catalysts in the literatures for advanced Li-S batteries.

Host material	Capacity (mAh g^{-1}) (current rate)	(cycles, current rate)	Decay rate (per cycle, %)	Ref
CoSA-N_3PS	1057 (0.2C)	(1000, 1C)	0.038%	11
Fe_3C/NC	1379 (0.1C)	(240, 1C)	0.090%	16
Ni-CF	1363 (0.1C)	(150, 0.1C)	0.201%	17
Mo_2C/CHS	1441 (0.1C)	(300, 1C)	0.060%	18
FeN_2-CN	1348 (0.2C)	(500, 1C)	0.055%	19
FeN_4-NC	~1245 (0.2C)	(500, 1C)	0.094%	19
Co-N_2	1004 (0.1C)	(700, 0.5C)	0.05%	20
Co-N_4	951 (0.1C)	(380, 0.5C)	NA	20
ZnTe@NC	1005 (0.1C)	(500, 1C)	0.15%	21
S@Fe-SAs/N-C_v	**1527 (0.1C)**	**(600, 1C)**	**0.023%**	**This work**

References

1 P. Hohenberg, W. Kohn, *Phys. Rev.,* 1964, **155,** B864−B871.

2 V. Wang, N. Xu, J. Liu, G. Tang, W. Geng, *Comput. Phys. Commun.,* 2017, **267,** 108033.

3 J. Perdew, K. K. Burke, M. Ernzerhof, *Phys. Rev. Lett.,* 1996, **77,** 3865.

4 P. E. Blochl, *Phys. Rev. B.,* 1994, **50,** 17953−17979.

5 S. Grimme, S. Ehrlich, L. Goerigk, *J. Comput. Chem.,* 2011, **32,** 1456−1465.

6 A. V. Krukau, O. A. Vydrov, A. F. Izmaylov, G. E. Scuseria, *J. Chem. Phys.,* 2006, **125,** 224106.

7 T. D. Kuehne, M. Iannuzzi, M. Del Ben, V. V. Rybkin, P. Seewald, F. Stein, T. Laino, R. Z. Khaliullin, O. Schuett, F. Schiffmann, D. Golze, J. Wilhelm, S. Chulkov, M. H. Bani-Hashemian, V. Weber, U. Borstnik, M. Taillefumier, A. S. Jakobovits, A. Lazzaro, H. Pabst, T. Mueller, R. Schade, M. Guidon, S. Andermatt, N. Holmberg, G. K. Schenter, A. Hehn, A. Bussy, F. Belleflamme, G. Tabacchi, A. Gloess, M. Lass, I. Bethune, C. J. Mundy, C. Plessl, M. Watkins, J. VandeVondele, M. Krack, J. Hutter, *J. Chem. Phys.,* 2020, **152,** 194103.

8 Q. He, X. Liao, L. Xia, Z. Li, H. Wang, Y. Zhao, D. G. Truhla, *J. Phys. Chem. C,* 2019, **123,** 20737–20747

9 T. Lu, F. Chen, *J. Comput. Chem.,* 2012, **33,** 580–592.

10 H. Li, Z. Huang, P. Qian, Y. Wang, R. Gao, A. Bendounan, H. Wang, Z. Chen, H. Zeng, G. Li, *Adv. Funct. Mater.,* 2024, 2419837.

11 C. Dong, C. Ma, C. Zhou, Y. Yu, J. Wang, K. Yu, A. Zheng, M. Gong, X. Xu, L. Mai, *Adv. Mater.,* 2024, 2407070.

12 K. Chen, Y. Zhu, Z. Huang, B. Han, Q. Xu, X. Fang, J. Xu, *ACS Nano,* 2024, **18,** 34791–34802.

13 F. Zhang, Z. Tang, T. Zhang, H. Xiao, H. Zhuang, P. Han, L. Zheng, L. Jiang, Q. Gao, *Angew. Chem. Int. Ed.,* 2024, e202418749.

14 Y. Zhang, C. Kang, W. Zhao, Y. Song, J. Zhu, H. Huo, Y. Ma, C. Du, P. Zuo, S. Lou, G. Yin, *J. Am. Chem. Soc.,* 2023, **145,** 1728-1739.

15 C. Huang, J. Yu, C. Y. Zhang, Z. Cui, J. Chen, W.-H. Lai, Y.-J. Lei, B. Nan, X. Lu, R. He, L. Gong, J. Li, C. Li, X. Qi, Q. Xue, J. Y. Zhou, X. Qi, L. Balcells, J. Arbiol, A. Cabot,

Adv. Mater., 2024, **36,** 2400810

16 C. Zhou, X. Li, H. Jiang, Y. Ding, G. He, J. Guo, Z. Chu, G. Yu, *Adv. Funct. Mater.,* 2021, **31,** 2011249.

17 Y. Tsao, H. Gong, S. Chen, G. Chen, Y. Liu, T. Z. Gao, Y. Cui, Z. Bao, *Adv. Energy Mater.,* 2021, **11,** 2101449.

18 J. Qian, Y. Xing, Y. Yang, Y. Li, K. Yu, W. Li, T. Zhao, Y. Ye, L. Li, F. Wu, *Adv. Mater.,* 2021, **33,** 2100810

19 J. Wang, W. Qiu, G. Li, J. Liu, D. Luo, Y. Zhang, Y. Zhao, G. Zhou, L. Shui, X. Wang, Z. Chen, Energy Storage Mater., 2022, **46,** 269-277.

20 D. Fang, P. Sun, S. Huang, Y. Shang, X. Li, D. Yan, Y. Von Lim, C. Su, B. Su, J. Juang, H. Yang, *ACS Mater. Lett.,* 2022, **4,** 1-10.

21 C. Huang, J. Yu, C. Li, Z. Cui, C. Zhang, C. Zhang, B. Nan, J. Li, J. Arbiol, A. Cabot, *Adv. Funct. Mater.,* 2023, **33,** 2305624.